GDCh Research Article Angewandte International Edition Chemie www.angewandte.org

How to cite: Angew. Chem. Int. Ed. 2024, e202413413
doi.org/10.1002/anie.202413413

Supramolecular Chemistry

A Supramolecular-Nanocage-Based Framework Stabilized by π-π Stacking Interactions with Enhanced Photocatalysis

*Jian-Hua Mei[+], Shan Lai[+], Yun-Nan Gong[+], Wen-Jie Shi, Ji-Hua Deng, Tong-Bu Lu, and Di-Chang Zhong**

Abstract: π frameworks, defined as a type of porous supramolecular materials weaved from conjugated molecular units by π-π stacking interactions, provide a new direction in photocatalysis. However, such examples are rarely reported. Herein, we report a supramolecular-nanocage-based π framework constructed from a photoactive Cu(I) complex unit. Structurally, 24 Cu(I) complex units stack together through π-π stacking interactions, forming a truncated octahedral nanocage with sodalite topology. The inner diameter of the nanocage is 2.8 nm. By sharing four open faces, each nanocage connects with four equivalent ones, forming a 3D porous π framework (**π-2**). **π-2** shows good thermal and chemical stability, which can adsorb CO_2, iodine, and methyl orange molecules. More importantly, **π-2** can serve as a photocatalyst for hydrogen evolution reaction. With ultrafine Pt subnanometer particles (0.9 ± 0.1 nm) incorporated into the nanocages as a co-catalyst, the hydrogen evolution rate reaches a record-high value of 524012 μmol/g_{Pt}/h in the absence of any additional photosensitizers. The high photocatalytic activity can be ascribed to the ultrafine size of the Pt particles, as well as the fast electron transfer from **π-2** to the highly active Pt upon illumination. **π-2** represents the unique stable supramolecular-cage-based π framework with excellent photocatalytic activity.

Introduction

Photocatalysis has shown potential applications in areas of sterilization, pollutant degradation, energy conversion, and so on,[1] where one of the most crucial components is the photocatalyst. Most heterogeneous photocatalysts have no definite crystal structures, which impedes the revealing of the performance-structure correlation and catalysis mechanism.[2] Well-defined crystal structures of photocatalysts facilitate to analyze and demonstrate the generation of photogenerated electron and holes, their transfer paths, as well as the final catalytic reactions. It is therefore highly desiring to get heterogeneous photo-catalysts with definite crystal structures.

Self-assembly has been found an effective mean to obtain heterogeneous photocatalysts with definite crystal structures, of which the construction of photoactive metal-organic frameworks (MOFs) and covalent organic frameworks (COFs) by coordination/covalent bonds have been extensively studied.[3] Besides, supramolecular porous frameworks, defined as a type of porous materials assembled from molecular monomers by noncovalent interactions, have also currently attracted considerable interest in photocatalysis.[4] For supramolecular porous frameworks, the structure design can be achieved in a molecular level; specific function groups can be easily introduced to the molecular monomers, by which the photocatalytic activity of the assembled supramolecular porous frameworks can be well tuned and improved. Among supramolecular porous frameworks, π frameworks stabilized merely by intermolecular π-π stacking interactions, are more suitable and promising in photocatalysis. Because the molecular monomers for constructing π frameworks are usually conjugated aromatic molecular units, the fabricated π frameworks are often photoactive, which well meets the most fundamental requirement of photocatalysts. However, as the π-π stacking is a type of weak noncovalent interactions, the fabrication of stable π frameworks is a big challenge. Therefore, very limited π frameworks were assembled and reported.[5] Especially in photocatalysis, there is only one π framework assembled from a Zn(II) complex unit was reported to be photoactive in CO_2 reduction.[5b]

Based on the above considerations, as well as the fact that cage-based porous materials facilitate to confine active species for enhancing photocatalysis,[6] we devoted to obtaining supramolecular-cage-based π frameworks with photoactivity. Fortunately, we got such a π framework based on bathocuproine (Bcp), a photoactive organic ligand with multiply conjugate aromatic moieties. Structurally, the metal center Cu(I) coordinates with two Bcp ligands, firstly forming a photoactive mononuclear Cu(I) complex of $[Cu(Bcp)_2]^+$ (Scheme 1). Then 24 $[Cu(Bcp)_2]^+$ complex ions stack together merely through π-π stacking interactions, to form a truncated octahedral nanocage with sodalite topology, with the inner diameter of 2.8 nm and the window size of 1.6 nm when corrected for van der Waals radii. By sharing four open faces, each nanocage connects with four

[*] J.-H. Mei,[+] S. Lai,[+] Dr. Y.-N. Gong,[+] Dr. W.-J. Shi, Dr. J.-H. Deng, Prof. Dr. T.-B. Lu, Prof. Dr. D.-C. Zhong
MOE International Joint Laboratory of Materials Microstructure, Institute for New Energy Materials and Low Carbon Technologies, School of Materials Science and Engineering, Tianjin University of Technology, Tianjin 300384, China
E-mail: dczhong@email.tjut.edu.cn

[+] These authors contributed equally

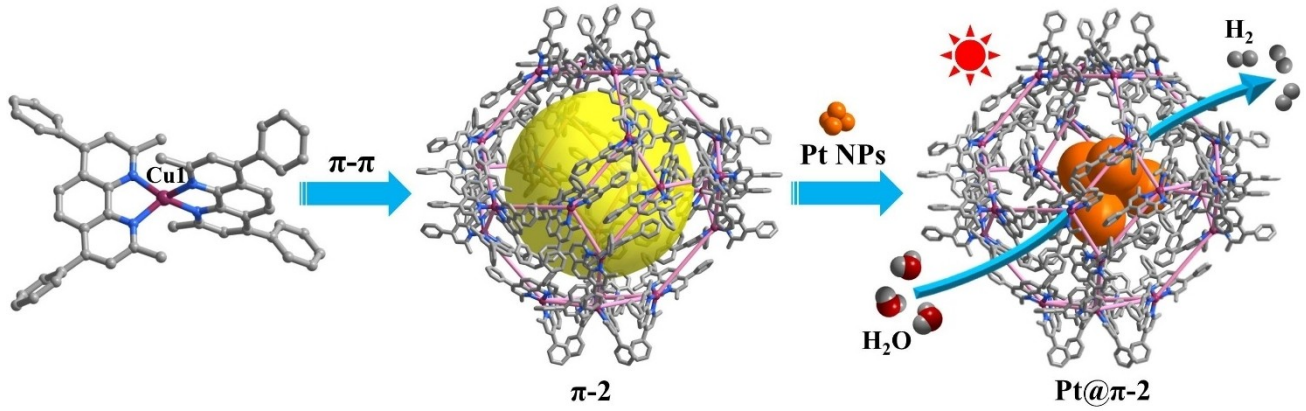

Scheme 1. Schematic illustration for the supramolecular assembly of **π-2** via π-π stacking interactions, and the photocatalytic hydrogen evolution of **Pt@π-2**.

equivalent ones, eventually forming a 3D porous π framework (**π-2**). **π-2** possesses good stability, which can adsorb CO_2, iodine and methyl orange molecules. Furthermore, benefiting from the good visible-light response of $[Cu(Bcp)_2]^+$ monomer, **π-2** can serve as a photocatalyst for hydrogen evolution reaction. With ultrafine Pt subnanometer particles (0.9 ± 0.1 nm) incorporated into the nanocages as a co-catalyst, the hydrogen evolution rate reaches as high as 524012 μmol/g_{Pt}/h in the absence of any additional photosensitizers (Scheme 1), showing the best activity among reported crystalline catalysts in photochemical hydrogen evolution.

Results and Discussion

Deep purple mircocrystals of **π-2** were afforded by evaporation of the red clear solution resulted from the solvothermal reaction of $Cu(Ac)_2{\cdot}H_2O$ and bathocuproine (Bcp) in DMF/H_2O at 100 °C. The electrospray ionization-mass spectroscopy (ESI-MS) of the microcrystals of **π-2** dissolved in acetonitrile shows a high-intensity ion peak at *m/z* 783.76, corresponding to the signal of $[Cu(Bcp)_2]^+$, which suggests that the species of **π-2** in solution is $[Cu(Bcp)_2]^+$ (Figure S1). Recrystallization of the microcrystals in DMF afforded polyhedral crystals of **π-2** suitable for single-crystal X-ray diffraction analysis (Figure S2). Single crystal X-ray diffraction analyses revealed that **π-2** crystallizes in cubic $Fd\bar{3}$ space group, with the crystal axis length of 56.9725(2) Å (see the Supporting Information; Tables S1–2). In the asymmetric unit, the metal center Cu(I) coordinates with four N atoms of two Bcp ligands, forming a mononuclear Cu(I) complex unit of $[Cu(Bcp)_2]^+$ (Figure 1a). The Cu(I) shows a tetrahedral coordination geometry, with the four N atoms situating the four vertexes and the Cu(I) locating the center of the tetrahedron (Figure S3). Well-known that the tetrahedral geometry is the typical geometry of Cu(I) in copper complexes. The Cu–N bond lengths range from 2.0278(16) to 2.0395(17) Å, similar to the values of Cu–N in reported Cu(I) complexes with tetrahedral geometry.[7] 24 of $[Cu(Bcp)_2]^+$ are held together through supramolecular interactions, generating a truncated octahedral supramolecular nanocage $[Cu(Bcp)_2]_{24}^{24+}$ (Figure 1b), with the inner diameter as large as 2.8 nm (Figure S4). The nanocage contains 24 vertexes and 14 faces. All these vertexes and faces are originated from the truncation to the six vertexes of the octahedron. The 24 vertexes are occupied by 24 Cu(I) ions (Figure 1b). The 14 faces involve 6 tetragonal faces and 8 hexagonal faces (Figures 1c and S4). The tetragonal and hexagonal faces consist of 4 and 6 $[Cu(Bcp)_2]^+$ units, respectively (Figure 1d–f). Note that the 4 tetragonal faces are covered with Bcp ligands (Figure 1d), while for the hexagonal faces, 4 of which are covered with Bcp ligands (Figure 1e), and the rest 4 are open, with the window size of 1.6 nm (Figures 1f and S4).

The supramolecular interactions holding $[Cu(Bcp)_2]^+$ structural units together to form the truncated octahedral supramolecular nanocage are deserved to be mentioned. After thoroughly analyzing the formation of the nanocage, we observed that only π-π stacking interactions contribute to the stabilization of the nanocage. As mentioned above, there is 14 faces in each nanocage, including 6 tetragonal faces and 8 hexagonal faces. The 6 tetragonal faces are closed. Each consists of 4 $[Cu(Bcp)_2]^+$ units linked together dependent on three pairs of offset face-to-face π-π stacking interactions, with the centroid distances (D) of $D_{Cg5\cdots Cg10}=3.8980(12)$ Å, $D_{Cg10\cdots Cg4}=3.8363(12)$ Å and $D_{Cg8\cdots Cg6}=3.6451(17)$ Å (Figure 1d; Table S3). Among the 8 hexagonal faces, 4 of which are closed. Each closed hexagonal face is composed with 6 $[Cu(Bcp)_2]^+$ units linked together dependent on not only offset face-to-face π-π stacking interactions, but also edge-to-face π-π stacking interactions (Figure 1e); the former is one and a half pairs of Cg10···Cg1 and Cg8···Cg6 stacking interactions, with the D of 4.0709(12) and 3.6451(17) Å, respectively, and the latter is one and a half pairs of C26-H26···Cg3 and C44-H44···Cg9 stacking interactions, with the H···Cg distances of 2.92 and 2.47 Å, respectively (Figure 1e; Tables S3–4). Besides the 4 closed hexagonal faces, there are 4 open hexagonal faces in each nanocage. As shown in Figure 1f, each open hexagonal face consists of 6 $[Cu(Bcp)_2]^+$ units linked through π-π stacking interactions, with $D_{Cg8\cdots Cg6}=3.6451(17)$ Å, $D_{Cg5\cdots Cg10}=3.8980(12)$ Å, and

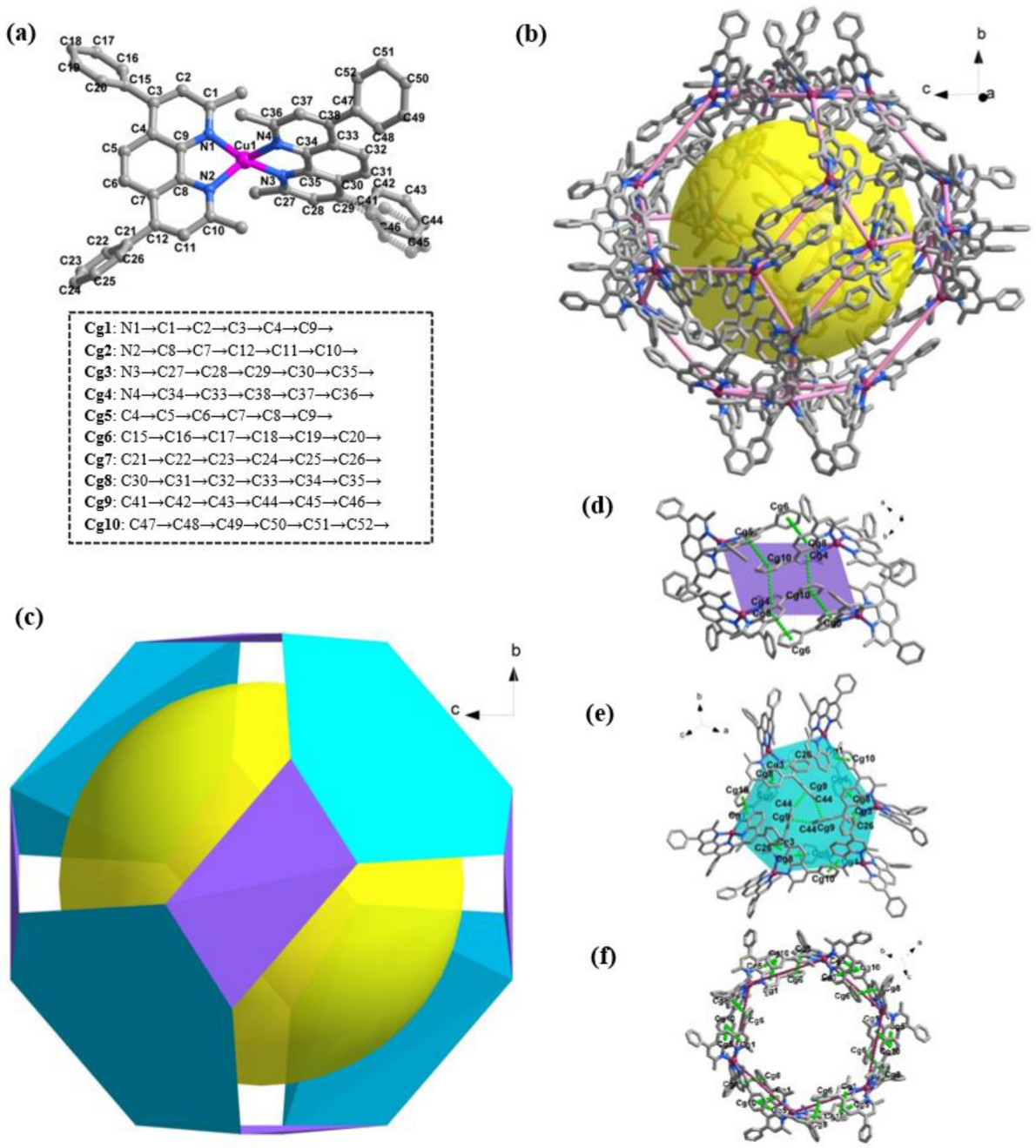

Figure 1. (**a**) Molecular structure of $[Cu(Bcp)_2]^+$ in **π-2** and the potential aromatic rings that may take part in π-π stacking interactions during self-assembly process. (**b**) Truncated octahedron nanocage in **π-2** formed by 24 $[Cu(Bcp)_2]^+$ units (The yellow sphere stands for the large cavity). (**c**) Polyhedron drawing of the truncated octahedron nanocage in **π-2**, in which 4 hexagonal faces are open. (**d**) Tetragonal face formed by 4 $[Cu(Bcp)_2]^+$ units linked through π-π stacking interactions (the distances (*D*) between ring centroids: $D_{Cg5\cdots Cg10}=3.8980(12)$ Å; $D_{Cg10\cdots Cg4}=3.8363(12)$ Å; $D_{Cg8\cdots Cg6}=3.6451(17)$ Å). (**e**) Hexagonal face formed by 6 $[Cu(Bcp)_2]^+$ units linked through π-π and C–H···π stacking interactions ($D_{Cg10\cdots Cg1}=4.0709$-(12) Å; $D_{Cg8\cdots Cg6}=3.6451(17)$ Å; $D_{C26\text{-}H26\cdots Cg3}=2.92$ Å; $D_{C44\text{-}H44\cdots Cg9}=2.47$ Å). (**f**) Hexagonal open face (open window) formed by 6 $[Cu(Bcp)_2]^+$ units linked through π-π stacking interactions ($D_{Cg8\cdots Cg6}=3.6451(17)$ Å; $D_{Cg5\cdots Cg10}=3.8980(12)$ Å; $D_{Cg1\cdots Cg10}=4.0709(12)$ Å).

$D_{Cg1\cdots Cg10}=4.0709(12)$ Å, respectively (Tables S3–4). These multiple π-π stacking interactions contribute to the formation of the supramolecular nanocage by holding 24 of $[Cu(Bcp)_2]^+$ structural units together.

The adjacent nanocages are linked together through sharing the open hexagonal faces (Figure 2a–b). As each nanocage has 4 open hexagonal faces, each nanocage connects with 4 equivalent ones by sharing the four open hexagonal faces (Figure 2c; Video S1), forming a 3D supramolecular-nanocage-based porous framework, as shown in the topological structure of **π-2** (Figure 2d). Note that with the exception of π-π stacking interactions, there is

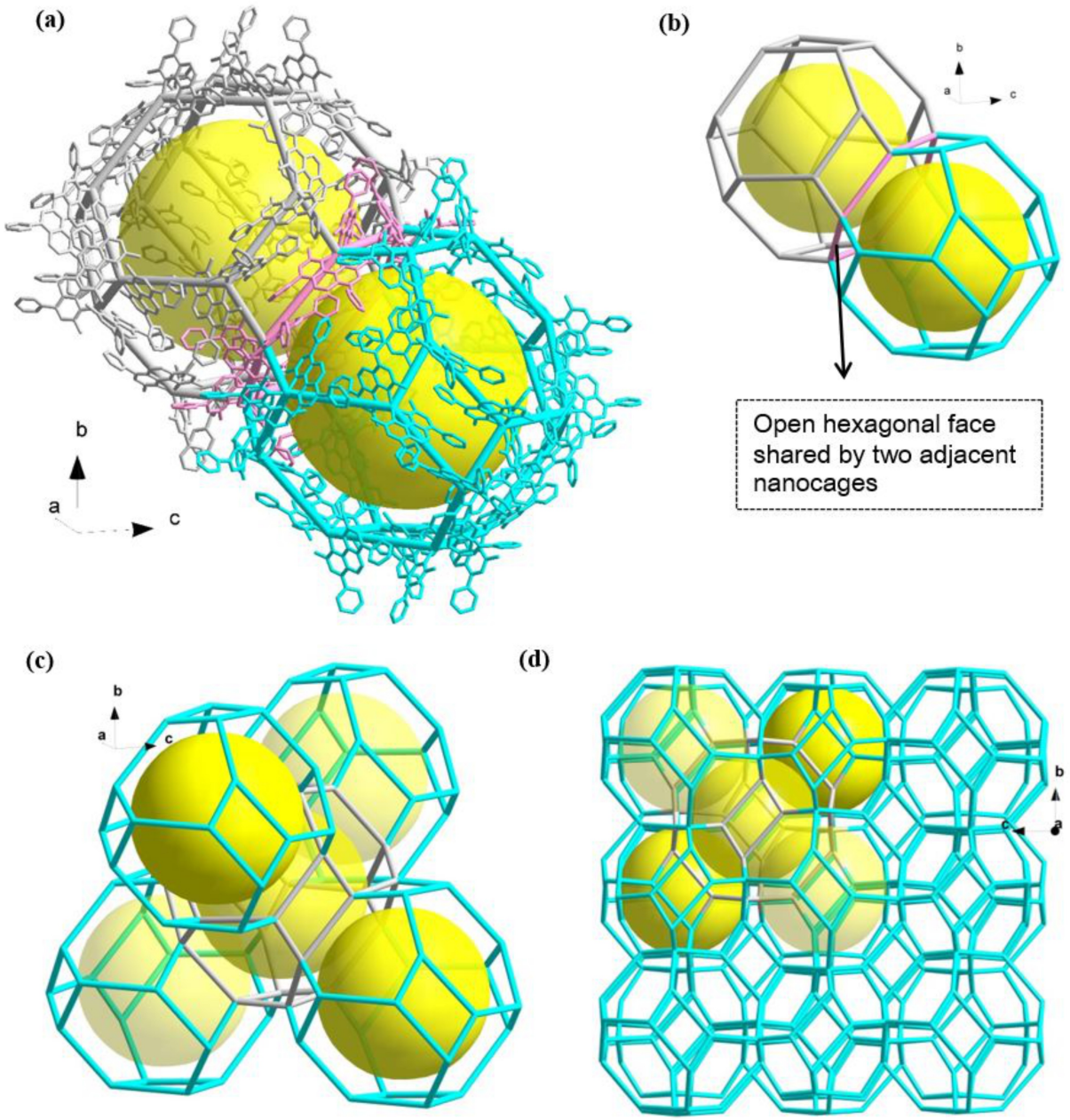

Figure 2. (**a**) Two adjacent truncated octahedron nanocages are linked together by sharing an open hexagonal face (in pink color), showing the connection mode between nanocages. (**b**) The connection of two simplified nanocages, clearly showing the shared open hexagonal face (the pink ring). (**c**) Each truncated octahedron cage links with four equivalent cages by sharing four open hexagonal faces. (**d**) Topological structure showing the 3D supramolecular-cage-based porous structure of **π-2.**

no other covalent/noncovalent interactions between $[Cu(Bcp)_2]^+$ structural units. Therefore, **π-2** is a rare π framework containing supramolecular nanocages. The intermolecular interactions between $[Cu(Bcp)_2]^+$ structural units were quantitatively calculated using energy decomposition analysis (see the Supporting Information). The results show that dispersion force dominates the total interactions, with the energy of −129.04 kJ/mol (Figure S5).

The powder X-ray diffraction (XRD) of **π-2** showed that all the peaks displayed in the pattern closely match with those in the simulated one generated from the single crystal diffraction data, indicating that single phase of **π-2** was formed (Figure S6). Scanning electron microscope (SEM) measurements confirmed the polyhedral morphology of **π-2** (Figure S7). X-ray photoelectron spectroscopy (XPS) measurements showed that the binding energy of Cu $2p_{3/2}$ in **π-2** is 932.1 eV (Figure S8a). This result, coupled with the kinetic energy of 915.5 eV for Cu LMM in the Auger electron spectroscopy (AES, Figure S8b), indicates that the oxidation state of copper in **π-2** is +1.[8] Thus each Cu(I) complex unit ($[Cu(Bcp)_2]^+$) is positively univalent, in agreement with the above results of the single-crystal X-ray diffraction analysis

and ESI-MS measurements. Ion chromatography analysis exhibited a signal at retain time of ca. 4.18 min, which suggests that the counter-anion in **π-2** is $HCOO^-$ (Figure S9). The appearance of Cu(I) and $HCOO^-$ in **π-2** may be due to the redox reaction of Cu(II) with DMF. In solvothermal condition, DMF often decomposes to generate $NH(CH_3)_2$ and CO. The latter could reduce Cu(II) to Cu(I) during the in situ construction of **π-2**.[9] Based on the these results, as well as those of infrared spectra (Figure S10), thermogravimetric analysis (Figure S11) and elemental analysis (see Supporting Information), the formula of **π-2** can be determined as $\{[Cu(Bcp)_2](HCOO)\}\cdot\{2DMF\cdot 8H_2O\}$.

Thermogravimetric (TG) analysis indicated that the guest molecules in **π-2** can be released when heated to 160 °C. Then no weight loss was observed till to 220 °C (Figure S11). The powder XRD patterns of **π-2** after activation are similar to those before activation (Figure S12), preliminarily proving the integrity of the porous framework of **π-2**. Variable-temperature powder XRD patterns of **π-2** showed that with the increase of temperatures, the diffraction peaks at 2θ over 2.5° gradually weaken, while the one at 2.5° does not change, even the temperature over 90 °C (Figure S13). Structurally, the diffraction peak at 2θ of 2.5° corresponds to the (111) crystal facet of **π-2**, that is, the open hexagonal faces (Figure S14), which indicates that the nanocage windows and pore structure of **π-2** were not destroyed after activation. The ^{1}H magic angle spinning nuclear magnetic resonance (^{1}H MAS NMR) spectroscopy measurements were carried out to further illustrate the structural integrity of **π-2**. As shown in Figure S15, the ^{1}H MAS NMR spectra of **π-2** after activation is almost the same as that before activation, well demonstrating the framework integrity of **π-2** after activation. This result was further confirmed by gas sorption tests (see the Supporting Information). As shown in Figure S16a and b, although the desolvated **π-2** can not adsorb N_2 and Ar, it can uptake CO_2 at diverse temperatures. For example, at 195 K, the adsorption amount of CO_2 reaches 79.02 cm^3/g, solidly evidencing the permanent porosity in **π-2**. Based on this adsorption isotherm, the pore distribution of 1–3 nm could be estimated (Figure S16c), which is consistent with the pore size measured from the crystal structure. It should be noted that at any tested temperature, the sorption isotherms assume large hysteresis. This may be ascribed to the special quadrupole moment of CO_2 (-1.4×10^{-39} C m^2). It has been reported that the quadrupole moment of CO_2 can induce the framework to interact with CO_2 molecules, thus increase the CO_2 binding and adsorption.[10] Besides good thermal stability, **π-2** also shows good chemical stability in H_2O and low-polarity organic solvents (see the Supporting Information). After immersed in several tested solvents for 24 h, the framework of **π-2** can retain intact (Figure S17). Moreover, **π-2** shows good stability in acidic and basic aqueous solution (pH 3–13; Figure S18). The good chemical stability of **π-2** may be ascribed to the Bcp ligands around the Cu(I) centre, which can provide a hydrophobic environment and protect the Cu–N bonds from being attacked by $H^+/OH^-/H_2O$. It is well-known that π-π stacking interaction is a type of weak noncovalent interaction (<2.0 kJ/mol) in supramolecular chemistry. Getting stable porous supramolecular frameworks dependent on merely π-π stacking interactions is still a great challenge. The emergence of **π-2**, a supramolecular-nanocage-based π framework, will give researchers new insights on weak supramolecular interactions. The concept of collective weakness making strength is also suitable for construction of stable porous supramolecular materials.

Because of the good stability, the capacities of **π-2** for encapsulating guest molecules were tentatively tested. First, the iodine capture by **π-2** was investigated (see the Supporting Information). The results show that **π-2** can not only capture the iodine in organic solution (I_2), but also in aqueous solution (I_3^-). As shown in Figure S19a, the adsorption of **π-2** to I_2 in *n*-hexane solution can be directly and clearly observed by the color of solution, which quickly changes from dark purple, to light purple and colorless with the increase of the soaking time. The corresponding UV/Vis spectra show the consistent results, where the I_2 adsorption peak at 522 nm quickly decreases with the soaking time. Particularly, at the initial 5 minutes, the adsorption peak sharply decreases (Figure S19b). This result indicates that the I_2 adsorption rate is very fast at the beginning. Quantitatively, on the basis of the standard curve of I_2 in *n*-hexane (Figure S20), the I_2 concentration decreases from 10.0 to 0.5 mM after **π-2** so aked for 3 min and to 0.04 mM for 20 min (Figure S19c), indicating that almost all the I_2 (99.6 %) in the *n*-hexane has been captured by **π-2**. Besides the fast adsorption dynamics to I_2, **π-2** also shows high iodine uptake. In I_2-KI aqueous solution, the iodine uptake of **π-2** can reach as high as 1.8 g/g (Figure S21). The adsorption kinetics and uptake capacity of **π-2** to iodine is obviously superior to most reported porous materials.[11] The excellent iodine uptake of **π-2** can be attributed to the large pore volume and the interactions between the aromatic rings of **π-2** and iodine.[12] The large cavity of **π-2** was further assessed by adsorption of methyl orange, a dye molecule with molecular size of ~1.3 nm (see the Supporting Information). As shown in Figure S22, the cavities of **π-2** can accommodate methyl orange molecules, which can also be detected by the color change and UV/Vis spectra. The color of the methyl orange aqueous solution gradually changes from orange red to orange, and finally to nearly colorless after 48 h (Figure S22a). The corresponding UV/Vis spectra show that the characteristic peak of methyl orange at 465 nm nearly disappeared (Figure S22b). All these observations indicate that almost all the methyl orange in solution has been adsorbed by **π-2**. According to the standard curve of methyl orange in aqueous solution (Figure S23), the methyl orange concentration decreases from 311.7 to 37.6 μM after **π-2** soaked for 24 h and to 6.5 μM for 48 h, corresponding to 97.9 % methyl orange in aqueous solution captured by **π-2** (Figure S22c).

The powder XRD measurements show that the patterns of **π-2** after either iodine capture or methyl orange encapsulation are similar to those of simulated one (Figures S24–25), illustrating that **π-2** can keep stable after encapsulation of iodine and methyl orange. The Auger electron spectroscopy (AES) measurement of **π-2** after iodine adsorption shows that the valence of the copper in **π-**

2 is still +1, which indicates that the Cu(I) will not be oxidized by the adsorbed I_2 (Figure S26). The above results solidly confirm that **π-2** possesses good stability and permanent porosity. **π-2** also shows good regeneration capacity in iodine and methyl orange capture. For the **π-2** adsorbed with I_2, about 97 % I_2 was released in 30 mL ethyl ether (Figure S27). For the **π-2** adsorbed with methyl orange, about 93 % methyl orange was released in 30 mL H_2O (Figure S28). The regenerated **π-2** can be further used to capture iodine and methyl orange via soaking (Figures S29–30). The powder XRD patterns of the regenerated **π-2** after two runs of capture-release processes for iodine or methyl orange are similar to those of as synthesized (Figures S31–32), indicating the good stability of **π-2** during the process of iodine and methyl orange adsorption, and the good regeneration capacity of **π-2** as an adsorbent. With good thermal and chemical stability, **π-2** can be highly dispersed in a mixture of CH_3OH and H_2O ($v:v=9:1$), which was preliminarily demonstrated by Tyndall effect (Figure S33). The dispersed nanoparticles of **π-2** in solution were confirmed by transmission electron microscopy (TEM). As shown in Figure S34, the particle size is about 16 nm, corresponding to about 10 supramolecular nanocages assembled together (Figure S35). The result of solid UV/Vis diffuse reflectance spectroscopy (DRS) demonstrates that **π-2** can adsorb light at a broad UV/Vis region of 200–800 nm (Figure S36).

The potential application of **π-2** was explored in photocatalytic hydrogen evolution, with Pt nanoparticles (NPs) as a co-catalyst. The ultrafine Pt NPs were firstly incorporated into the nanopores of **π-2** by a hydrazine vapor reduction method, resulting in **Pt@π-2** composite catalyst (see the Supporting Information). TEM images showed that the Pt NPs have been completely incorporated into the nanopores of **π-2**, with particle size around 0.9 ± 0.1 nm (Figures 3 and S37). The energy dispersive spectroscopy (EDS) mapping reveals the homogeneous distribution of C, N, Cu, and Pt in **Pt@π-2** (Figure S38). This was further confirmed by electron tomographic reconstruction, which clearly demonstrated the uniform 3D distribution of ultrafine Pt NPs throughout the interior nanopores of **π-2** (Video S2). The content of Pt in **Pt@π-2** is 0.78 wt %, as determined by inductively coupled plasma-mass spectrometry (ICP-MS) analysis.

The photocatalytic activity of the above catalysts for hydrogen evolution was evaluated in NaOH aqueous solution, by using 3-dimethyl-2-phenyl-2,3-dihydro-1H-benzo[d]-imidazole (BIH) as a sacrificial agent, and 300 W Xe lamp ($\lambda > 320$ nm) as an illuminant (see the Supporting Information). It was found that **π-2** itself really possesses photocatalytic activity for water splitting, with the H_2 generation rate of 150.8 μmol/g/h (Figure 4; Table S5, Entry 1). After confinement of ultrafine Pt NPs, the resulted **Pt@π-2** composite catalyst displays much enhanced photo-

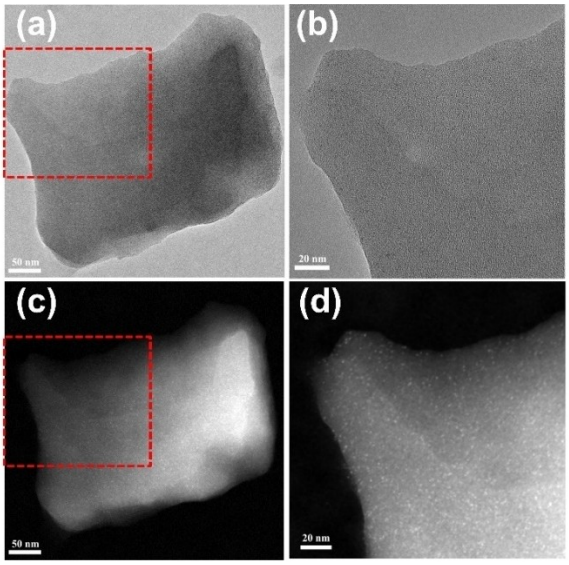

Figure 3. (**a**) and (**b**), TEM images of **Pt@π-2**. (**c**) and (**d**), HAADF-STEM images of **Pt@π-2**.

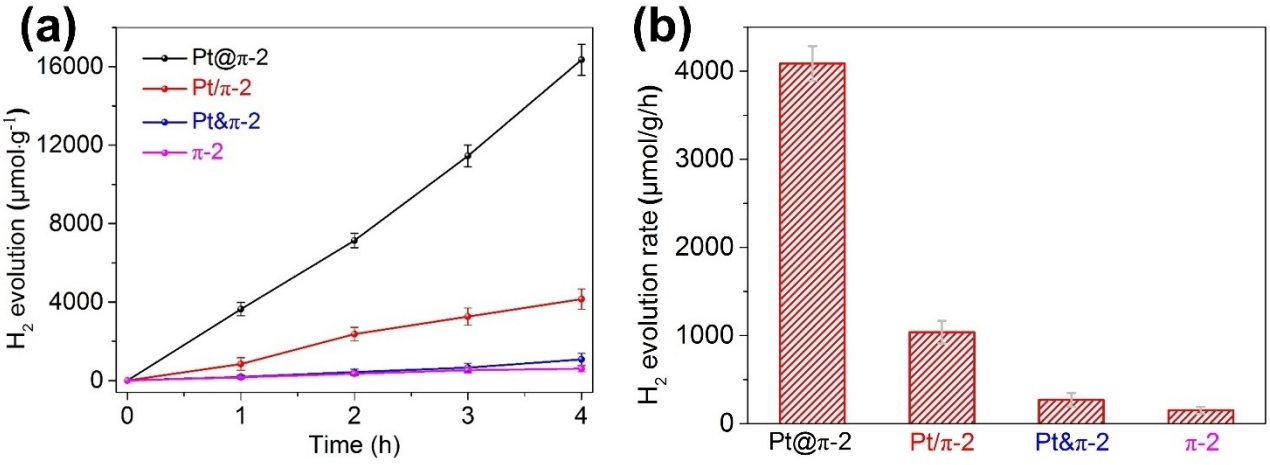

Figure 4. (**a**) Time-dependent photocatalytic activity of **Pt@π-2**, **Pt/π-2**, **Pt&π-2**, and **π-2** for H_2 evolution in 0.01 M NaOH aqueous solution. (**b**) Comparison of the photocatalytic activity of **Pt@π-2**, **Pt/π-2**, **Pt&π-2**, and **π-2**. Reaction conditions: 1.0 mg catalyst, 0.01 M NaOH aqueous solution (4 mL), 0.01 M BIH, 300 W Xe lamp ($\lambda > 320$ nm) for 4 h at 25 °C. The error bars were obtained by three repeated experiments.

catalytic activity. The H_2 generation rate reaches as high as 4087.3 μmol/g/h (Figure 4; Table S5, Entry 2), much higher than those of Pt NPs (6.9 μmol/g/h) and **π-2** (150.8 μmol/g/h) under the same condition (Table S5, Entry 1–3). Based on the amount of Pt, the hydrogen evolution rates were calculated to be an unprecedented value of 524012 $\mu mol/g_{Pt}/h$ ($\lambda > 320$ nm) and 117822 $\mu mol/g_{Pt}/h$ ($\lambda > 420$ nm). These values would make **Pt@π-2** a unique photocatalyst among reported crystalline photocatalysts for hydrogen evolution (Table S6).[13] The extremely high photocatalytic activity of **Pt@π-2** may be ascribed to the ultrafine size of Pt NPs. The ultrafine size not only endows the Pt with high activity, but also enable the Pt highly to disperse onto the surface of the nanopore of **π-2** and make full use of Pt in photocatalytic hydrogen evolution. In addition, the extremely high photocatalytic activity of **Pt@π-2** also indicates that the Pt NPs within the nanopores of **π-2** could effectively promote the separation of the photo-generated electron and hole in **π-2**, thus greatly boosting the hydrogen evolution. It should be noted that the highly photocatalytic performance was achieved in the absence of any additional photosensitizers, which highlights **π-2** is really an excellent photocatalyst.

Control experiments demonstrated that without **Pt@π-2**, BIH or light illumination, no H_2 was detected, indicating that all these factors are indispensable to the photocatalytic hydrogen evolution (Table S5, Entry 4–6). Besides excellent activity, **Pt@π-2** also exhibits good durability for photocatalytic hydrogen evolution. As shown in Figure S39, after four catalytic cycles, the photocatalytic activity of **Pt@π-2** in hydrogen evolution does not show remarkable reduce. The Pt content, powder XRD patterns, and morphologies of **Pt@π-2** after cyclic reactions are similar to those of **Pt@π-2** freshly prepared (Table S7, and Figures S40–41), which further confirms the robustness of **Pt@π-2**. In addition, it was found that there were negligible Pt and Cu contents in the reaction solution after four runs of photocatalytic hydrogen evolution (Table S7), and almost no Bcp ligand was detected in this reaction solution (Figure S42). These observations further evidence that **Pt@π-2** is a robust photocatalyst for hydrogen evolution. We also checked the possible photocatalytic activity of the reaction solution after four runs of photocatalytic hydrogen evolution reactions (**Pt@π-2** was removed by centrifugation), the result shows that negligible H_2 was detected (Table S8). This result not only evidences the robustness of **Pt@π-2**, but also elucidates that the photocatalytic hydrogen evolution reaction over **Pt@π-2** occurs in the solid-state, rather than solution-state.

To explore the effect of pore confinement of **π-2** on the photocatalytic activity, **Pt/π-2**, in which most Pt NPs were deposited on the outer surface of **π-2** and the Pt content is similar to that in **Pt@π-2**, was prepared by a liquid reduction method (see the Supporting Information; Figure S43a). Additionally, **Pt&π-2**, physical mixture of pre-synthesized Pt NPs and **π-2**, where all Pt NPs were deposited outer surface of **π-2** and the Pt content is similar to that in **Pt@π-2**, was also obtained (see the Supporting Information; Figure S44a). The photocatalytic activity of both **Pt/π-2** and **Pt&π-2** for hydrogen evolution was tested under the same catalytic condition as **Pt@π-2**. The results show that the hydrogen evolution rates of **Pt/π-2** and **Pt&π-2** are 1038.3 and 269.7 μmol/g/h, respectively (Figure 4; Table S5, Entry 7–8). These values are much lower than that of **Pt@π-2** (4087.3 μmol/g/h), which illustrates that the pore confinement of **π-2** to the Pt NPs is important for the photocatalytic activity. In addition, **Pt/π-2** and **Pt&π-2** show obviously lower stability than **Pt@π-2**; it was observed that the particle size of Pt obviously become bigger after photocatalysis compared with those freshly prepared (Figures S43b and 44b), despite the powder XRD patterns of **Pt/π-2** and **Pt&π-2** are similar to those freshly prepared (Figures S45–46). Therefore, the pore confinement could not only contribute to obtain ultrafine Pt NPs with high activity and durability, but also reinforce the interfacial interactions between the pore surface and Pt NPs, thus facilitate for the electron transfer from **π-2** to Pt NPs. In addition, the photocatalytic hydrogen generation test of the physically mixed Pt NPs, Bcp and Cu(I) (Pt&Bcp&Cu(I); Table S5, Entry 9) was also carried out. The results show that Pt&Bcp&Cu(I) has photocatalytic activity for hydrogen evolution, with the hydrogen evolution rate of 90.8 μmol/g/h, also much lower than that of **Pt@π-2** (4087.3 μmol/g/h). This observation suggests that the coordination assembly of Cu(I) and Bcp is beneficial for enhancing the photocatalytic hydrogen evolution activity.

To estimate the thermodynamic driving force and elucidate the possible catalytic mechanism, the (photo−)redox potentials of the bare $[Cu(Bcp)_2]^+$ complex were determined by UV/Vis absorption, emission spectra and cyclic voltammetry (CV), (Figures S47–48).[14] As shown in Table S9, the oxidation potential of BIH was more negative than the excited-state reduction potential of $[Cu(Bcp)_2]^+$*, implying that the thermodynamic driving force is enough for BIH to transfer electron to excited $[Cu(Bcp)_2]^+$*.[15] This indicates a reductive quenching mechanism for $[Cu(Bcp)_2]^+$*. Thus, the possible reaction pathways of **Pt@π-2**, **Pt/π-2** and **Pt&π-2** for H_2 evolution were proposed. Upon illumination, $[Cu(Bcp)_2]^+$ was excited to produce $[Cu(Bcp)_2]^+$*, which was quenched by BIH to form $[Cu(Bcp)_2]$. The resulting $Cu(Bcp)_2]$ transfers electrons to Pt NPs, where the adsorbed H^+ was reduced to H_2.[15b,16]

The photoluminescence (PL) spectra, photocurrent, and electrochemical impedance spectroscopy (EIS) of **Pt@π-2**, **Pt/π-2**, **Pt&π-2** and **π-2** were further measured (see the Supporting Information). The PL spectra of **Pt@π-2**, **Pt/π-2** and **Pt&π-2**, especially for **Pt@π-2**, show significantly damped emission in contrast to **π-2**, indicating that the recombination of the photogenerated electrons and holes is enormously restrained after introduction of Pt NPs (Figure 5a). Transient fluorescence spectroscopy measurements demonstrated that the PL lifetimes of **Pt@π-2**, **Pt/π-2**, **Pt&π-2** and **π-2** are 604, 416, 350 and 244 ps, respectively (Figure 5b, Table S10). These results further illustrate that the introduced Pt NPs could serve as an electron reservoir, effectively separating the photogenerated electrons and holes, and thus boosting the photocatalytic hydrogen evolution. The photocurrent response tests showed that the current density of **Pt@π-2**, **Pt/π-2**, and **Pt&π-2** is higher than that of **π-2**. Particularly for **Pt@π-2**, the current density is

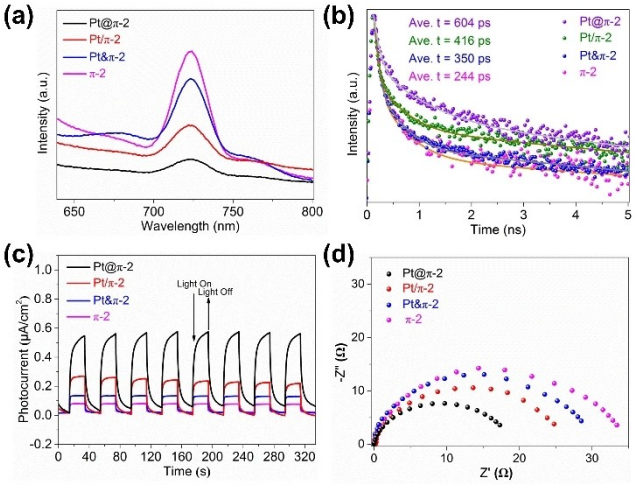

Figure 5. (**a**) PL spectra (λ_{Ex} = 480 nm), (**b**) Time-resolved photoluminescence decays, (**c**) photocurrent response, and (d) Nyquist plots of **Pt@π-2**, **Pt/π-2**, **Pt&π-2**, and **π-2**.

over several times higher than that of **π-2** (Figure 5c). This observation further suggests that the photogenerated electron concentration in **Pt@π-2** is higher than in **π-2**, and the better separation efficiency of photogenerated electrons and holes in **Pt@π-2**. EIS spectra show that the arc radius of **Pt@π-2** is smaller than those of **Pt/π-2**, **Pt&π-2** and **π-2** (Figure 5d), indicating that the charge transfer resistance of **Pt@π-2** is lower than those of **Pt/π-2**, **Pt&π-2** and **π-2**, also benefits for the activity enhancement. In all, besides the ultrafine size of the Pt NPs, the strengthened visible-light absorption, accellerated electron transfer, as well as the high separation efficiency of photogenerated electrons and holes enable **Pt@π-2** possess the best photocatalytic activity for hydrogen evolution.

Conclusion

In summary, with a self-assembly approach, a unique stable supramolecular-nanocage-based photocatalyst has been constructed by merely intermolecular π-π stacking interactions, which shows good stability, permanent porosity and excellent photocatalytic performance. Structurally, 24 mononuclear Cu(I) complexes stack together through π-π stacking interactions, forming a truncated octahedral nanocage with sodalite topology. The inner diameter of the nanocage is 2.8 nm and the window size is 1.6 nm when corrected for van der Waals radii. By sharing four open faces, each nanocage connects with four equivalent nanocages, resulting in a 3D porous π framework (**π-2**). More importantly, **π-2** can serve as a photocatalyst for hydrogen evolution reaction. With ultrafine Pt subnanometer particles (0.9 ± 0.1 nm) incorporated into the nanocages as a co-catalyst, the hydrogen evolution rate reaches a record-high value of 524012 μmol/g_{Pt}/h in the absence of any additional photosensitizers. The high photocatalytic activity can be ascribed to the ultrafine size of the Pt particles, as well as the fast electron transfer from **π-2** to highly active Pt sites upon illumination. **π-2** represents the unique stable supramolecular-cage-based π framework with excellent photocatalytic activity.

Acknowledgements

This work was supported by the National Key R&D Program of China (2022YFA1502902), the National Natural Science Foundation of China (22271218, 22071182, 22371208, and 21931007). We acknowledge Dr. Yong-Liang Huang at Shantou University for the single-crystal structural analysis.

Conflict of Interest

The authors declare no conflict of interest.

Data Availability Statement

The data that support the findings of this study are available in the supplementary material of this article.

Keywords: Supramolecular nanocage · π framework · π-π stacking · photocatalysis · hydrogen evolution reaction

[1] H. Wang, Y.-M. Tian, B. Konig, *Nat. Chem. Rev.* **2022**, *6*, 745–755.
[2] a) H.-L. Wu, X.-B. Li, C.-H. Tung, L.-Z. Wu, *Adv. Mater.* **2019**, *31*, e1900709; b) J. Wang, Y.-X. Feng, M. Zhang, C. Zhang, M. Li, S.-J. Li, W. Zhang, T.-B. Lu, *CCS Chem.* **2020**, *2*, 81–88; c) Y. Wang, X. Wang, M. Antonietti, *Angew. Chem. Int. Ed.* **2012**, *51*, 68–89.
[3] a) G.-X. Lan, Y.-J. Fan, W.-J. Shi, E. You, S.-S. Veroneau, W.-B. Lin, *Nat. Catal.* **2022**, *5*, 1006–1018; b) G.-X Lan, Z. Li, S.-S. Veroneau, Y.-Y. Zhu, Z.-W. Xu, C. Wang, W.-B. Lin, *J. Am. Chem. Soc.* **2018**, *140*, 12369–12373; c) Y. Kamakura, C. Suppaso, I. Yamamoto, R. Mizuochi, Y. Asai, T. Motohashi, D. Tanaka, K. Maeda, *Angew. Chem. Int. Ed.* **2023**, *62*, e202305923; d) Z.-B. Fang, T.-T. Liu, J.-X. Liu, S.-Y. Jin, X.-P. Wu, X.-Q. Gong, K.-C. Wang, Q. Yin, T.-F. Liu, R. Cao, H.-C. Zhou, *J. Am. Chem. Soc.* **2020**, *142*, 12515–12523; e) L.-Z. Dong, L. Zhang, J. Liu, Q. Huang, M. Lu, W.-X. Ji, Y.-Q. Lan, *Angew. Chem. Int. Ed.* **2020**, *59*, 2659–2663; f) Y.-N. Gong, X.-Y. Guan, H.-L. Jiang, *Chem. Rev.* **2023**, *475*, 214889; g) M. Lu, J. Liu, Q. Li, M. Zhang, M. Liu, J.-L. Wang, D.-Q. Yuan, Y.-Q. Lan, *Angew. Chem. Int. Ed.* **2019**, *58*, 12392–12397; h) J.-W. Wei, L. Zhao, C. He, S.-J. Zheng, J.-N.-H. Reek, C.-Y. Duan, *J. Am. Chem. Soc.* **2019**, *141*, 12707–12716.
[4] a) Q.-X. Zhou, Y. Guo, Y.-F. Zhu, *Nat. Catal.* **2023**, *6*, 574–584; b) A.-A. Zhang, D.-H. Si, H.-B. Huang, L. Xie, Z.-B. Fang, T.-F. Liu, R. Cao, *Angew. Chem. Int. Ed.* **2022**, *61*, e202203955; c) B.-Q. Yu, T. Meng, X. Ding, X.-L. Liu, H.-L. Wang, B.-T. Chen, T.-Y. Zheng, W. Li, Q.-D. Zeng, J.-Z. Jiang, *Angew. Chem. Int. Ed.* **2022**, *61*, e202211482; d) B.-Q. Yu, L.-J. Li, S.-S. Liu, H.-L. Wang, H.-Y. Liu, C.-X. Lin, C. Liu, H. Wu, W. Zhou, X.-Y. Li, T.-Y. Wang, B.-L. Chen, J.-Z. Jiang, *Angew. Chem. Int. Ed.* **2021**, *60*, 8983–8989; e) Q. Yin, E.-V. Alexandrov, D.-H. Si, Q.-Q. Huang, Z.-B. Fang, Y. Zhang, A.-A.

Zhang, W.-K. Qin, Y.-L. Li, T.-F. Liu, D.-M. Proserpio, *Angew. Chem. Int. Ed.* **2022**, *61*, e202115854.
[5] a) H.-L. Zhu, H.-Y. Chen, Y.-X. Han, Z.-H. Zhao, P.-Q. Liao, X.-M. Chen, *J. Am. Chem. Soc.* **2022**, *144*, 13319–13326; b) J.-H. Zhang, Y.-N. Gong, H.-J. Wang, Y.-C. Wang, W. Yang, J.-H. Mei, D.-C. Zhong, T.-B. Lu, *Proc. Natl. Acad. Sci. USA* **2022**, *119*, e2118278119; c) C. Chen, Z.-Y. Di, H. Li, J.-Y. Liu, M.-Y. Wu, M.-C. Hong, *CCS Chem.* **2021**, *3*, 1352–1362; d) G.-L. Li, Z. Zhuo, B. Wang, X.-L. Cao, H.-F. Su, W. Wang, Y.-G. Huang, M.-C. Hong, *J. Am. Chem. Soc.* **2021**, *143*, 10920–10929; e) D. Meng, J.-L. Yang, C.-Y. Xiao, R. Wang, X.-F. Xing, O. Kocak, Y. Yang, *Proc. Natl. Acad. Sci. USA* **2020**, *117*, 20397–20403; f) J.-H. Deng, J. Luo, Y.-L. Mao, S. Lai, Y.-N. Gong, D.-C. Zhong, T.-B. Lu, *Sci. Adv.* **2020**, *6*, eaax9976.
[6] a) G.-A. Leith, C.-R. Martin, J.-M. Mayers, P. Kittikhunnatham, R.-W. Larsen, N.-B. Shustova, *Chem. Soc. Rev.* **2021**, *50*, 4382–4410; b) X.-C. Yang, J.-K. Sun, M. Kitta, H. Pang, Q. Xu, *Nat. Catal.* **2018**, *1*, 214–220; c) J.-S. Wang, K. Wu, C. Yin, K. Li, Y. Huang, J. Ruan, X. Feng, P. Hu, C.-Y. Su, *Nat. Commun.* **2020**, *11*, 4675; d) N.-N. Sun, C.-M. Wang, H.-L. Wang, L. Yang, P. Jin, W. Zhang, J.-Z. Jiang, *Angew. Chem. Int. Ed.* **2019**, *58*, 18011–18016.
[7] a) M.-T. Miller, P, -K. Gantzel, T.-B. Karpishin, *J. Am. Chem. Soc.* **1999**, *121*, 4292–4293; b) L. Lemus, J. Guerrero, J. Costamagna, R. Lorca, D.-H. Jara, G. Ferraudi, A. Oliver, A.-G. Lappin, *Dalton Trans.* **2013**, *42*, 11426–11435.
[8] T.-T. Zhuang, Y. Pang, Z.-Q. Liang, Z. Wang, Y. Li, C.-S. Tan, J. Li, C.-T. Dinh, P.-D. Luna, P.-L. Hsieh, E.-H. Sargent, *Nat. Catal.* **2018**, *1*, 946–951.
[9] a) S. Ding, N. Jiao, *Angew. Chem. Int. Ed.* **2012**, *51*, 9226–9237; b) Y. Feng, K. Zhang, B. Yan, S.-M. Li, Y.-K. Du, *Catalyst* **2016**, *6*, 103.
[10] a) L. Bastin, P.-S. Brcia, E.-J. Hurtado, J.-C. Silva, A.-E. Rodrigues, B. Chen, *J. Phys. Chem. C* **2008**, *112*, 1575–1581; b) H.-S. Choi, M.-P. Suh, *Angew. Chem. Int. Ed.* **2009**, *48*, 6865–6869; c) P.-L. Llewellyn, S. Bourrelly, C. Serre, Y. Filinchuk, G. Férey, *Angew. Chem. Int. Ed.* **2006**, *45*, 7751–7754.
[11] W. Xie, D. Cui, S.-R. Zhang, Y.-H. Xu, D.-L. Jiang, *Mater. Horiz.* **2019**, *6*, 1571–1595.
[12] Z.-J. Yan, Y. Yuan, Y.-Y. Tian, D.-M. Zhang, G.-S. Zhu, *Angew. Chem. Int. Ed.* **2015**, *54*, 12733–12737.
[13] a) Q.-J. Mo, L. Zhang, S.-H. Li, H.-L. Song, Y.-N. Fan, C.-Y. Su, *J. Am. Chem. Soc.* **2022**, *144*, 22747–22758; b) W. Zhang, Y. Wang, J.-P. Guo, Y. Yu, W.-B. Duan, Y. Yang, X. Bai, B. Liu, *Nanoscale* **2021**, *13*, 10807–10815; c) Q. Zuo, T.-T. Liu, C.-S. Chen, Y. Ji, X.-Q. Gong, Y.-Y. Mai, Y.-F. Zhou, *Angew. Chem. Int. Ed.* **2019**, *58*, 10198–10203; d) S. Li, H.-M. Mei, S.-L. Yao, Z.-Y. Chen, Y.-L. Lu, L. Zhang, C.-Y. Su, *Chem. Sci.* **2019**, *10*, 10577–10585; e) J.-D. Xiao, L. Han, J. Luo, S.-H. Yu, H.-L. Jiang, *Angew. Chem. Int. Ed.* **2018**, *57*, 1103–1107; f) X.-Z. Fang, Q.-C. Shang, Y. Wang, L. Jiao, T. Yao, Y.-F. Li, Q. Zhang, Y. Luo, H.-L. Jiang, *Adv. Mater.* **2018**, *30*, 1705112; g) T. He, S.-M. Chen, B. Ni, Y. Gong, Z. Wu, L. Song, L. Gu, W.-P. Hu, X. Wang, *Angew. Chem. Int. Ed.* **2018**, *57*, 3493–3498; h) Y.-F. Chen, L.-L. Tan, J.-M. Liu, S. Qin, Z.-Q. Xie, J.-F. Huang, Y.-W. Xu, L.-M. Xiao, C.-Y. Su, *Appl. Catal. B* **2017**, *206*, 426–433; i) J.-D. Xiao, Q.-C. Shang, Y.-J. Xiong, Q. Zhang, Y. Luo, S.-H. Yu, H.-L. Jiang, *Angew. Chem. Int. Ed.* **2016**, *55*, 9389–9393; j) M.-C. Wen, K. Mori, T. Kamegawa, H. Yamashita, *Chem. Commun.* **2014**, *50*, 11645–11648; k) T.-H. Zhou, Y.-H. Du, A. Borgna, J.-D. Hong, Y.-B. Wang, J.-Y. Han, W. Zhang, R. Xu, *Energy Environ. Sci.* **2013**, *6*, 3229–3234.
[14] a) J.-W. Wang, Z. Li, Z.-M. Luo, Y. Huang, F. Ma, S. Kupfer, G. Ouyang, *Proc. Natl. Acad. Sci. USA* **2023**, *120*, e2221219120; b) K.-K. Chen, S. Guo, H. Liu, X. Li, Z.-M. Zhang, T.-B. Lu, *Angew. Chem. Int. Ed.* **2020**, *59*, 12951–12957.
[15] a) P. Wang, S. Guo, Q.-P. Zhao, S.-Y. Xu, H. Lv, T.-B. Lu, Z.-M. Zhang, *Angew. Chem. Int. Ed.* **2024**, *63*, e202312450; b) M. Ming, H. Yuan, S. Yang, Z. Wei, Q. Lei, J. Lei, Z. Han, *J. Am. Chem. Soc.* **2022**, *144*, 19680–19684.
[16] P. Wang, S. Guo, H.-J. Wang, K.-K. Chen, N. Zhang, Z.-M. Zhang, T.-B. Lu, *Nat. Commun.* **2019**, *10*, 3155.

Manuscript received: July 16, 2024
Accepted manuscript online: September 7, 2024
Version of record online: ■■, ■■

Research Article

Supramolecular Chemistry

J.-H. Mei, S. Lai, Y.-N. Gong, W.-J. Shi, J.-H. Deng, T.-B. Lu, D.-C. Zhong* _____ **e202413413**

A Supramolecular-Nanocage-Based Framework Stabilized by π-π Stacking Interactions with Enhanced Photocatalysis

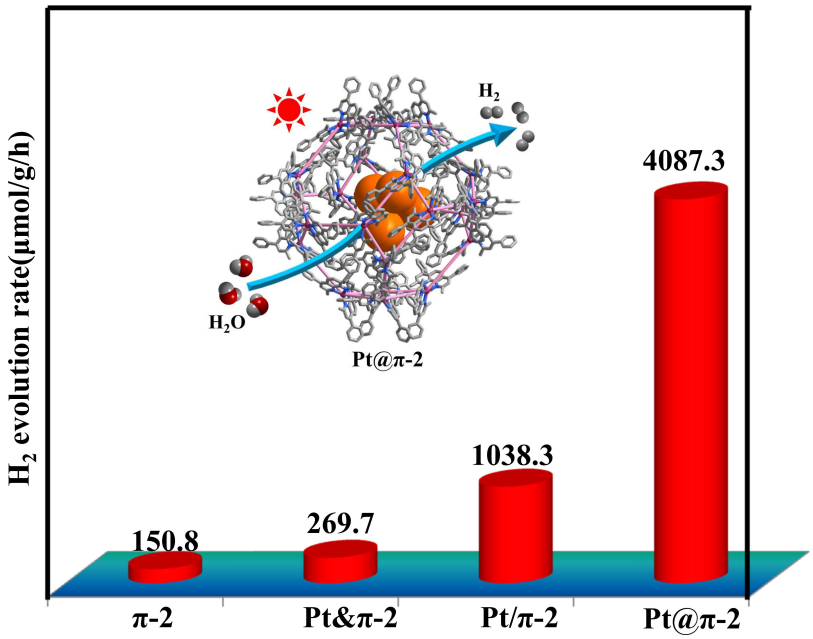

A supramolecular-nanocage-based π framework was firstly reported, which can serve as an efficient photocatalyst for hydrogen evolution reaction in the absence of any additional photosensitizers. The H_2 evolution rate reaches as high as 524012 μmol/g_{Pt}/h.